Pergamon

Geochimica et Cosmochimica Acta, Vol. 64, No. 19, pp. 3347–3355, 2000

0016-7037/00 $20.00 + .00

PII S0016-7037(00)00424-5

Hydrous species geospeedometer in rhyolite: Improved calibration and application

YOUXUE ZHANG,[1,*] ZHENGJIU XU,[1] and HARALD BEHRENS[2]

[1]Department of Geological Sciences, University of Michigan, Ann Arbor, Michigan 48109-1063, USA
[2]Institut für Mineralogie, Universität Hannover, D-30167 Hannover, Germany

(*Received October* 27, 1999; *accepted in revised form March* 6, 2000)

Abstract—The hydrous species geospeedometer is based on the homogeneous interconversion reaction between molecular H_2O species and OH species in silicate melts and glasses. Here we report new data for the calibration of the geospeedometer in rhyolitic glass, extending the coverage of quench rate to 94 K/s and of H_2O_t to 7.7 wt.% by using a piston-cylinder apparatus at low pressures (200–500 MPa) to prevent bubble growth and to generate high and monitored quench rates. The new experimental data at pressure are highly reproducible and consistent with earlier data at 0.1 MPa, indicating negligible pressure effect on the relation between speciation and quench rate at $P \leq 500$ MPa. In order to avoid calibration uncertainties, the original infrared data are used to represent species concentrations and the equilibrium constant. $\bar{A}_{523}$ and $\bar{A}_{452}$ (absorbances of the 523 and 452 mm^{-1} bands in terms of peak height per mm sample thickness) are used to represent concentrations of molecular H_2O and OH groups, respectively, and Q' $(=\bar{A}^2_{452}/\bar{A}_{523})$ is used to represent the quotient of the species interconversion reaction, since there is rough proportionality between the corresponding parameters ($\bar{A}_{523}$ and molecular H_2O, $\bar{A}_{452}$ and OH, Q' and the quotient Q). Zhang et al. [Geochim. Cosmochim. Acta **61,** 3089–3100 (1997a)] showed that for a given quench rate (q), there is an excellent linear relation between ln Q' and $\ln(\bar{A}_{523} + \bar{A}_{452})$ when total H_2O is $\leq$3.0%. With new data at higher total H_2O, the linear relation does not hold anymore. Furthermore, the new data show that the linear relation between ln Q' and ln q does not hold at high q. Hence, the geospeedometry model of Zhang et al. can be used for interpolation, but extrapolation may lead to large errors. A new geospeedometry model using the combined data set is presented in this work and applied to natural rhyolitic glasses. The new geospeedometer can be used to quantify cooling rates in a quench medium or an experimental apparatus. Furthermore, it can be used to determine the cooling rates of individual pyroclasts, different parts of a lava flow, and melt inclusions in phenocrysts, thus allowing inference of rich details of volcanic processes. *Copyright © 2000 Elsevier Science Ltd*

1. INTRODUCTION

One of the basic aims of petrology and geochemistry is to infer the temperature–pressure–time history, including the cooling rate. Cooling rates of rocks can be estimated on the basis of an understanding of the kinetics of homogeneous reactions inside a phase (e.g., Mueller, 1967; Ganguly, 1982; Ganguly et al., 1994; Zhang, 1994a). The hydrous species reaction $H_2O_m + O \Leftrightarrow 2OH$ (where H_2O_m is a molecular H_2O, O is an anhydrous oxygen, and OH is a hydroxyl group associated with Si, Al, Na, etc.; Stolper, 1982a; 1982b) has been investigated extensively and its kinetics has been quantified to be applied as a geospeedometer for volcanic glasses. An accurate and practical geospeedometer may enrich future volcanological studies. For example, accurate determination of cooling rates of individual pyroclasts may be used to infer the flight history of pyroclasts and to constrain the eruption intensity and eruption column processes. For lava domes, knowledge of cooling rates of different layers can constrain whether the dome grew by endogeneous or exogeneous process: for endogeneous growth, the cooling rates should decrease from the surface to the interior; for exogeneous growth, there would be cycles in cooling rates reflecting new layers. For lava flows, cooling rate studies of lava at different depths may help constrain whether the flow was laminar or not. For laminar lava flows, it may be possible to use the geospeedometer to relate depth in a lava flow and cooling rates. Such a relation may provide a method to estimate lava thickness even if the top surface has been eroded away. In summary, there are many applications of the hydrous species geospeedometer in studying volcanological processes, and these applications may reveal new details of volcanological processes.

Zhang et al. (1995) carried out isothermal experiments at 0.1 MPa (1 bar) to investigate the kinetics of the reaction and found that the reaction mechanism is complex. That is, it is not straightforward to apply the results of isothermal kinetic studies to infer cooling rates. Hence, Zhang et al. (1997a) used a new strategy and carried out experiments to empirically calibrate the relation between cooling rate (q) and H_2O_m and OH species concentrations so that the reaction can be used as a geospeedometer. Their calibration covered the cooling rate range from 0.000 17 to 1 K/s, and H_2O_t range from 0.5 to 3.0 wt.% (% indicates wt.% below unless otherwise specified). The upper limit on q is due to the limitations of the one-atmosphere furnace; more rapid quench (such as taking sample out of the furnace) cannot be quantitatively monitored. The upper limit on H_2O_t is to avoid bubbling during the experiments, again a problem owing to the use of one-atmosphere furnaces.

Because of the lack of a sound theoretical understanding of the reaction kinetics, extrapolation of the relation to infer greater quench rates and/or at greater H_2O_t may be problematic. Therefore it is necessary to extend the coverage to greater quench rates and H_2O_t contents. Here we report new data

* Author to whom correspondence should be addressed (youxue@umich.edu).

extending the coverage of quench rate to 94 K/s and of H_2O_t to 7.7%. The new experiments were carried out in a piston cylinder apparatus at 200 and 500 MPa pressure to prevent bubble formation. Although the piston-cylinder apparatus is not designed to work well in this pressure range, we succeeded in generating highly reproducible results that are consistent with the data of Zhang et al. (1997a). The combination of our new data and previously reported data covers quench rates from 0.000 17 K/s to 94 K/s and H_2O_t from 0.5% to 7.7%. We present an updated relation between quench rate and species concentrations for use as a geospeedometer. We also apply the geospeedometer to experimentally and naturally cooled hydrous rhyolitic glasses.

2. EXPERIMENTAL AND ANALYTICAL METHODS

The experimental procedures generally follow those of Zhang et al. (1997a), except that a piston-cylinder apparatus (instead of one-atmosphere furnaces) is used in this study. A cylindrical sample was heated to a high temperature and then cooled at the desired rate. Then the sample was doubly polished to remove the diffusive layer and analyzed by Fourier transform infrared spectroscopy (FTIR).

Four natural hydrous rhyolitic glasses with 0.8, 1.2, 1.8, and 2.4% H_2O_t (from Mono Craters, see Zhang et al., 1997a) and three synthetic rhyolitic glasses with 3.8%, 5.6%, and 7.7% H_2O_t were used. The synthetic rhyolitic glasses were prepared in an internally heated pressure vessel at University of Hannover by adding about 3%, 5%, and 7% H_2O to a natural rhyolitic glass (named KS sample with 0.7–0.8% H_2O_t). The H_2O_t contents of the synthetic glasses were determined by pyrolysis and subsequent Karl–Fischer titration, also at the University of Hannover. The major oxide concentrations of the rhyolitic glasses are reported in Zhang et al. (1997b).

The controlled cooling rate experiments and FTIR analyses were carried out at the University of Michigan. In order to prevent bubbling and to generate high and monitored cooling rate, a piston-cylinder apparatus was used for the experiments. Glass cylinders (typically 2.5 mm in diameter and 2.5 mm long) were prepared from the original glass chip. Species concentrations in the starting material were measured by IR. The cylinder was enclosed in a graphite capsule. The capsule was then placed in a sleeve of crushable Al_2O_3 and then in the center of a 32 mm long graphite heater. During the experiment, a type-D thermocouple was in touch with the top of the graphite capsule. The thermocouple was connected to both the controller and a data acquisition board for computer recording of the temperature history. Pressed and fired $BaCO_3$ (with 3% xerox toner as binder) cells served as both pressure medium and insulator.

Although the piston-cylinder apparatus is not designed for pressures of 200–500 MPa, we take advantage of the fact that speciation does not depend on pressure at $\leq$500 MPa (Zhang, 1994b), which is further confirmed in this study. Therefore, the main purpose of using the piston-cylinder apparatus is to apply some pressure to avoid bubbling for high-H_2O_t samples, and to generate high and quantitatively monitored quench rate. Nevertheless, we added a new analog pressure gauge so that lower pressures can be read more precisely (to 5 MPa). The pressurization procedure is as follows. The sample assembly is pressurized at room temperature to the required pressure, then heated to a relatively low temperature (about 100–250°C depending on the H_2O_t content of the sample, so that negligible H_2O is diffusively lost) for stress relaxation. When the pressure drops to more than ~10% below the required pressure, it is manually pumped to ~10% above the required pressure. This procedure is repeated until the pressure becomes stable. Hence the pressurizing procedure is both "piston-in" and "piston-out." Bubble growth is not a problem in any of the the experiments. That is, the applied pressure (and perhaps the kinetic barrier for bubble nucleation) is enough to prevent bubble growth during the experiments. Pressure is manually adjusted in later stages of the heating and cooling experiment if necessary.

After the pressure becomes stable, the sample temperature is rapidly (in about 30–60 s) increased to the desired experimental temperature, chosen to be at least 50 °C above the expected T_{ae} at the planned cooling rate, where T_{ae} is the apparent equilibrium temperature of the cooled glass, defined as the corresponding equilibrium temperature one calculates from the species distribution in a cooled glass (Ihinger et al., 1999) even though the species distribution does not reflect equilibrium at any single temperature (Zhang, 1994a). After a duration of 5–20 minutes, the sample is cooled down, either by programming the temperature controller at a specified cooling rate, or by turning off the power to the piston-cylinder furnace. In the former case, the temperature is linear to time with a constant cooling rate. In the latter case, the temperature varies with time nonlinearly resulting in a variable cooling rate. The cooling rate in both cases is obtained from recorded temperature history as the slope on the plot of temperature against time at $T = T_{ae}$ (see Zhang et al., 1997a). The greatest cooling rate at T_{ae} is achieved by turning off the power to the piston-cylinder and varies from 59 to 94 K/s.

The cooled sample is extracted from the assembly, and is found to maintain its shape with no breakage. It is subsequently doubly polished to remove the layers that have been affected by dehydration during the experiment. The thickness of such a layer to be removed is estimated from the diffusion studies of Zhang et al. (1991) and Zhang and Behrens (2000). The resulting doubly polished section is measured by FTIR (Nicolet 60SX) for species concentrations. The aperture diameter is typically 0.5 mm. The sample of 2.5 mm diameter disk is fixed on the aperture for IR measurement. On average, three to four points (i.e., spectra) are measured on the sample. All the measured points are sufficiently away from the rim to avoid influences of partially dehydrated layers at the rim. To achieve high precision, 1024 to 2048 scans are taken for each spectrum. The baseline of the IR spectrum is fit by a flexicurve. The peak height is used to represent the band intensity. The precision for band intensity is about 1% relative for each band. As will be discussed later, such a precision results in a precision of 30% for estimating cooling rates.

3. RESULTS

Seventeen experiments were carried out with 59 individual IR analyses. Data reported in Table 1 are averages of IR analyses of different points of the same sample. Because some samples are slightly heterogeneous, averaged data do not always reflect the high precision of band intensities (1% relative precision). Hence individual analyses are used in figures and data treatments. Relative uncertainties obtained from the fits are $\leq$4% for controlled cooling rate experiments and are $\leq$25% for quenching experiments by shutting off the power. Uncertainties for the thickness of glass wafers are 2 μm. T_{ae} ranges from 300°C to 700°C. The cooling rate at T_{ae} ranges from 0.0016 K to 94 K/s. The H_2O_t ranges from 0.8% to 7.7 wt.%. Because there are still some lingering uncertainties about the accuracy of the calibration in obtaining the species concentrations, especially at high H_2O_t (Zhang et al., 1997b; Zhang, 1999; Withers and Behrens, 1999), and since knowing the actual species concentrations is not essential to the prediction of cooling rates, we will use the band intensities directly in presenting the results so that (i) the accuracy of the original data is not compromised by the uncertainties in determining species concentrations and (ii) no later revisions to the geospeedometer will be necessary with revised calibration. Following Zhang et al. (1997a), we define

$$Q' = (\bar{A}_{452})^2/\bar{A}_{523}, \quad (1)$$

where $\bar{A}_{523}$ and $\bar{A}_{452}$ are, respectively, the absorbances of the 5230 and 4520 cm^{-1} bands (in terms of peak height) per mm sample thickness (i.e., $\bar{A}_{523} = A_{523}/d$ in Table 1). Because $\bar{A}_{523}$ and $\bar{A}_{452}$ are roughly proportional to H_2O_m and OH contents (Stolper, 1982a;b; Newman et al., 1986; Zhang et al., 1997b), Q' is roughly proportional to Q, $[OH]^2/\{[H_2O_m][O]\}$,

Table 1. Controlled cooling rate experimental data.

Sample	q K/s	P MPa	T_0 °C	A_{523}	A_{452}	d mm	H_2O_t wt.%	ln Q'	T_{ae} °C	q_c K/s
3aD2A-C1	0.670	200	850	0.336	0.291	1.206	2.37	−1.56	456	0.62
KS-C11	0.828	200	1000	0.084	0.261	1.888	0.839	−0.84	573	0.76
KS-C12	6.50	200	1000	0.067	0.243	1.725	0.830	−0.67	619	6.0
3b11C	65.9	200	800	0.300	0.473	2.002	1.84	−0.99	572	74
KS-C10	69.1	200	1100	0.095	0.451	3.215	0.791	−0.42	698	81
KS&3-C4	0.0016	500	405	0.591	0.244	0.99	3.8%	−2.28	352	0.0017
POB10-Cl	0.0168	500	1000	0.147	0.25	1.583	1.14	−1.31	475	0.016
KS&3-C3	0.0169	500	430	0.757	0.336	1.312	3.8%	−2.17	369	0.011
KS&5-C3	0.0164	500	400	0.836	0.237	0.864	5.6%	−2.55	331	0.019
KS&7-C3	0.0162	500	370	0.709	0.15	0.56	7.7%	−2.87	300	0.013
KS&5-C4	1.02	500	460	0.641	0.217	0.705	5.6%	−2.26	375	1.3
KS&7-C6	0.991	500	450	0.753	0.185	0.61	7.7%	−2.60	337	1.0
POB10-C2	94.3	500	1000	0.076	0.209	1.149	1.17	−0.71	624	57
3aD2A-C2	59.2	500	1000	0.436	0.459	1.653	2.55	−1.23	531	68
KS&3-C2	67.9	500	520	0.763	0.500	1.585	3.8%	−1.58	477	3.8
KS&5-C2	69.6	500	480	0.924	0.386	1.102	5.6%	−1.92	434	65
KS&7-C2	71.0	500	470	0.844	0.260	0.735	7.7%	−2.22	397	75

q: experimental quench rate at $T = T_{ae}$.
P: experimental pressure.
T_0: temperature at which the sample is initially held at (for about 10 minutes) before cooling.
T_{ae}: the apparent equilibrium temperature of the quenched sample calculated using Ihinger et al. (1999), $T_{ae} = (2660 + 89.6\ \bar{A}_{523} + 1082\ \bar{A}_{452})/(2.482 - \ln(\bar{A}_{452}{}^2/\bar{A}_{523}) - 273.15$.
A_{523} and A_{452}: absorbances of the 523 and 452 mm^{-1} bands.
d: thickness of the doubly polished wafer.
H_2O_t: total H_2O content calculated from Zhang et al. (1997b) except for KS&3, KS&5, and KS&7 which are analyzed by Karl–Fischer titration at Hannover.
Q': defined in Eqn. 1.
q_c: calculated cooling rate using Eqn. 5.

which equals the equilibrium constant K if equilibrium is reached and if species mix ideally. The relative uncertainty in Q' can be estimated from each spectrum to be 2% to 3%. That is, the uncertainty in ln Q' is 0.02 to 0.03. One of the disadvantages of using band intensities instead of species concentrations is that the true relation between Q, H_2O_t, and quench rate q may be obscured.

We first confirm that the relation between the quench rate and quenched speciation is independent of pressure within the investigated pressure range of 0.1–500 MPa. Three experiments, two at 200 MPa (3aD2A-C1 and KS-C11) and one at 500 MPa (POB 10-C1), were conducted to overlap with the 0.1 MPa data of Zhang et al. (1997a) in both H_2O_t and q. Figure 1 compares POB10-C1 (500 MPa) with 0.1 MPa experimental data on a ln Q' against ln ΣA plot (where ΣA denotes $\bar{A}_{523} + \bar{A}_{452}$ and is roughly proportional to H_2O_t content) for quench rates of ~0.0167 K/s, i.e., 1°C/min. (To highlight the unit difference, cooling rate per minute will be given as °C/min, and cooling rate per second will be given as K/s.) The small range of quench rates (~10% total variation) does not significantly affect the relation. It can be seen that data for the POB10-C1 sample (500 MPa) fall exactly on the trend defined by the 0.1 MPa data. The 200 MPa data also fall on the trend defined by the 0.1 MPa data (Fig. 2).

Zhang et al. (1997a) showed that when H_2O_t is less than 3.0% (roughly corresponding to ln ΣA of −0.50) the relation between ln Q' and ln ΣA is linear (dashed line in Fig. 1). Figure 1 shows that this linear correlation does not hold at greater H_2O_t. Figure 2 shows further that for other fixed quench rates, the relation between ln Q' and ln ΣA is nonlinear. The nonlinear trends suggest that the formulation of the relation between cooling rate and final species concentrations based on low H_2O_t data can only be used for interpolation but cannot be extrapolated to higher H_2O_t. Our data also show that for a

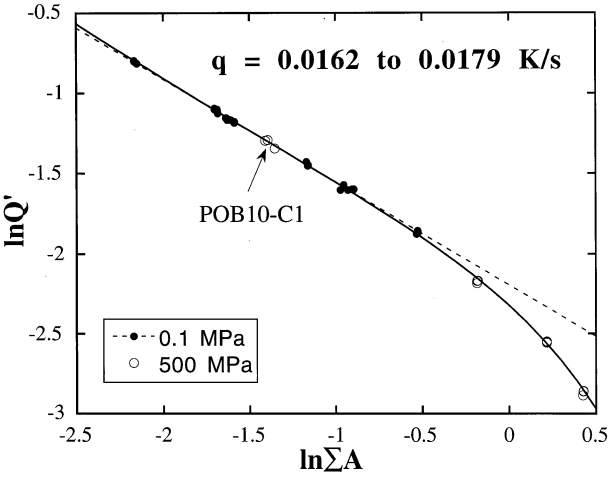

Fig. 1. The relation between ln Q' and ln ΣA at a single quench rate (1.02 ± 0.05°C/min). Recall that Q' is roughly proportional to the quotient Q and ΣA is roughly proportional to H_2O_t. The solid dots represent 0.1 MPa data from Zhang et al. (1997a). The open circles represent data from this work. The 500 MPa data of POB 10-C1 fall right on the trend defined by the 0.1 MPa data. The dashed line is a linear fit to the 0.1 MPa and low-H_2O_t data. The linear relation (Zhang et al., 1997a) does not hold at higher H_2O_t. The solid curve is a fit to all data and is described in the text.

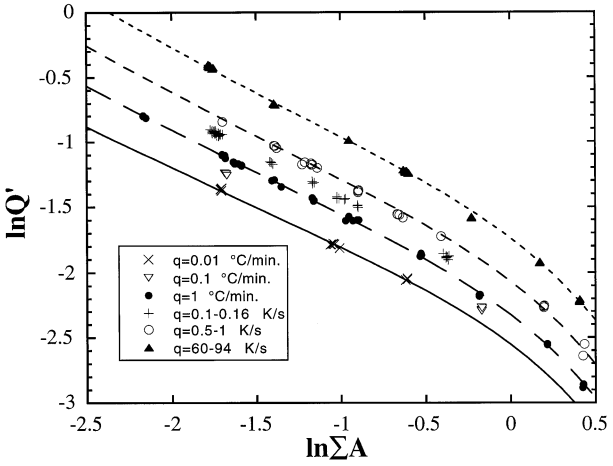

Fig. 2. The relation between ln Q' and ln ΣA at various quench rates. Most experimental data are shown in this figure except for those with cooling rates of 0.33 and 3.0°C/min (these data are not outliers, but for clarity they are not shown in this figure). The curves are fits to the data at $q = 0.01$°C/min (solid curve), 1°C/min (long-dashed curve), 1 K/s (medium-dashed curve), and 70 K/s (short-dashed curve) by Eqn. 3 as explained in the text. The high self-consistency and precision (very small scatter for data at each q) are evident.

given ΣA, the relation between ln Q' and ln q is not linear (Fig. 3).

4. DISCUSSION

4.1. An Empirical Relation Between Species Band Intensities and Cooling Rate

In this section we discuss the trends shown by the data and empirical methods for predicting cooling rates using our experimental calibration. Hereafter we combine the data from this work and the data from Zhang et al. (1997a) to examine the relations between Q', q, and ΣA. Figures 1 and 2 show that the shape of the dependence of Q' on ΣA is not linear and does not depend on q. The departure from the linear relation for the ln Q' vs. ln ΣA relation at H_2O_t greater than 3% may be partially due to the use of band intensities instead of the true species concentrations. First, $Q' = (\bar{A}_{452})^2/\bar{A}_{523}$ and $Q = [OH]^2/\{[H_2O_m][O]\}$ are not perfectly proportional to each other. Because the anhydrous oxygen concentration [O] decreases with increase H_2O_t (i.e., with increasing ΣA), a plot of ln Q vs. ln ΣA (instead of ln Q' vs. ln ΣA) may deviate less from the straight line. Second, the proportionality between ΣA and H_2O_t is imperfect because molar absorptivity for the 4520 cm^{-1} band does not equal to that of the 5230 cm^{-1} band (Newman et al., 1986; Zhang et al., 1997b). Third, the departure from the linear relation for the ln Q' vs. ln ΣA relation may also be partially attributed to the flexicurve fit to the baseline of the OH peak. If a single straight line is used to fit the baseline (Behrens et al., 1996), the OH band intensity would be greater at higher H_2O_t, which would partially offset the deviation from the linear trend. However, linear baseline also has problems. For example, in situ studies indicate that 4520 cm^{-1} band intensity variation with measurement temperature at a given OH content in the glass state is small with flexicurve baseline and much larger with linear baseline (Withers et al., 1999). Another complexity is that sometimes it is difficult to fit the high wave number side of the 5230 cm^{-1} band with a straight line. Currently, there is no objective way to obtain the true baseline. Hence the flexicurve fitting is adopted here for consistency with the earlier work on this geospeedometer (Zhang et al., 1997a).

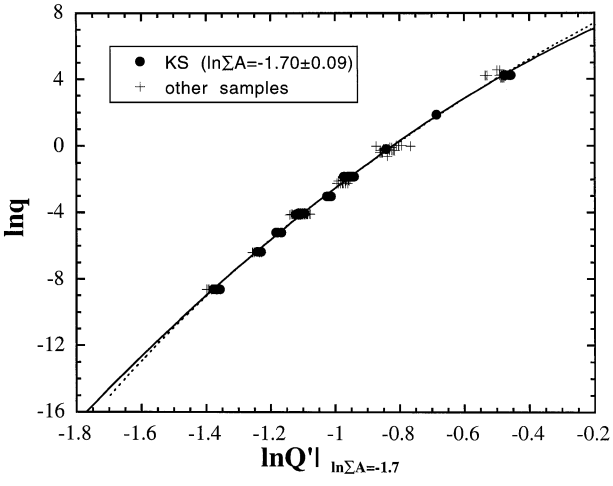

Fig. 3. The relation between ln q and ln $Q'|_{\ln \Sigma A=-1.7}$. The value of ln $Q'|_{\ln \Sigma A=-1.7}$ is calculated using Eqn. 4. The KS samples are shown in dots, and other samples (with ln ΣA from -2.2 to 0.4) are shown as pluses. The solid curve is a fit of all the data (KS and other samples) by a second-order polynomial with $\ln q = 8.7905 + 7.8096\ \xi - 3.4937\ \xi^2$, where $\xi = \ln Q'|_{\ln \Sigma A=-1.7}$. The dashed curve is calculated using Eqn. 3.

Because the relation between ln Q' and ln ΣA at low ΣA is linear but deviates from linearity at greater ΣA, at each fixed q we use the following expression to relate ln Q' and ln ΣA:

$$z = m_0 + m_1 x + m_2 \exp(m_3 x), \tag{2}$$

where $x = \ln \Sigma A$, $z = \ln\ Q'$, and m_0, m_1, m_2, and m_3 are constants to be found by fitting the data. The above equation works well at each q. In order to fit all the data, the following expression is found to work well:

$$z = m_0 + m_1 x + m_2 y + m_3 x\, y + m_4 \exp(m_5 x + m_6 y) + m_7 \exp(m_8 x) = f(x, y), \tag{3a}$$

where $y = \ln q$, and m_0, m_1, m_2, . . . , and m_8 are constants to be obtained by fitting the data. The fitting results for the constants by an unweighted nonlinear regression are

$$m_0 = -5.4276,\ m_1 = -1.196,\ m_2 = -0.044\,536,$$
$$m_3 = -0.023\,054,\ m_4 = 3.7339,\ m_5 = 0.213\,61,$$
$$m_6 = 0.030\,617,\ m_7 = -0.371\,19,\ m_8 = 1.6299.$$

The fits of the data are shown in Figs. 1 and 2. Equation 3 can also be written as

$$Q' = e^{m_0}(\Sigma A)^{m_1 + m_3 \ln q}\, q^{m_2} \exp[m_4(\Sigma A)^{m_5} q^{m_6} + m_7(\Sigma A)^{m_8}], \tag{3b}$$

to show how Q', q, and ΣA are related. Because the relative

error of each of Q', q, and ΣA is roughly constant, it is better to use Eqn. 3a instead of Eqn. 3b for unweighted regression.

Equation 3a is good for interpolation when used as a geospeedometer. In order to illustrate how all data points line up in a single curve, and to examine visually how the expression extrapolates, we compare the experimental data and the calculated relation between $\ln q$ and $\ln Q'$ at $x = \ln \Sigma A = -1.7$ (KS sample with total H_2O content of ~0.8%). This $\ln \Sigma A$ value is chosen because many data (especially those in Zhang et al., 1997a) are close to this $\ln \Sigma A$. For samples with $\ln \Sigma A \neq -1.7$, a correction was made in the following manner to account for the dependence of $\ln Q'$ on $\ln \Sigma A$:

$$\ln Q'|_{\ln \Sigma A=-1.7} = \ln Q' - f(x, y) + f(-1.7, y), \qquad (4)$$

where $f(x, y)$ is from Eqn. 3a. If such a correction accounts for the concentration dependence of $\ln Q'$, all data should follow a single trend. Figure 3 shows all experimental data (dots and pulses) and the calculated curve (dashed) using Eqn. 3a at $\ln \Sigma A = -1.7$. The small scatter around the curve for the KS sample (dots) indicates the measurement uncertainty and that for other samples (pluses) indicates the goodness of the correction using Eqn. 4. All the experimental data in Fig. 3 can also be well fit with the following second order polynomial:

$$\ln q = 8.7905 + 7.8096\xi - 3.4937\xi^2, \qquad (5)$$

where $\xi = \ln Q'|_{\ln \Sigma A=-1.7}$. Detailed examination shows that Eqns. 5 and 3 fit the data with the same precision. The average deviation of calculated $\ln q$ from the experimental data is 0.20 (22% relative for q) and the maximum deviation is 0.76 (a factor of 2 for q). The uncertainty in the inferred cooling rate caused by the uncertainty in the IR band intensities can be estimated from the above equations as follows. With a relative error of 1% for both bands, the error in $\ln q$ is about 0.3 (or 30% relative error in q) but it is somewhat dependent on Q' owing to the nonlinear term in Eqn. 5. If the relative error is 5% for both bands, the error in $\ln q$ is 1.5 (that is, a factor of 4.6 for q). Therefore, the average fitting error of 0.2 in obtaining $\ln q$ is roughly consistent with average IR band intensity uncertainty of ~1% relative. Figure 3 also shows that extrapolation of both Eqns. 3 and 5 up to 1000 K/s or down to 10°C/yr (3×10^{-7} K/s) gives similar results and there is no strange behavior (such as unexpected turns) of the curves. It should be noted that Eqn. 5 is not independent of Eqn. 3 since the correction in Eqn. 4 requires Eqn. 3.

There are two ways to solve $\ln q$ from $\ln Q'$ and $\ln \Sigma A$. One is to use Eqn. 3 by trial-and-error method. That is, varying the assumed $\ln q$ so that calculated $\ln Q'$ using Eqn. 3 and measured $\ln \Sigma A$ agrees with the measured $\ln Q'$. This works well when calculating several cooling rates. If there are many data, the easiest way is to use a spreadsheet program with the following iteration: using Eqn. 4 to calculate $\xi (= \ln Q'|_{\ln \Sigma A=-1.7})$ that depends on $\ln q$, and using Eqn. 5 to calculate $\ln q$ that depends on ξ. Because the latter method is more efficient, it is used hereafter to calculate q from species band intensities.

Figure 2 can also be used to infer the cooling rate. For convenience of use of this geospeedometer, we present Fig. 4 for quick estimation of cooling rates, in which the peak height of the 452 mm^{-1} band is plotted against that of the 523 mm^{-1} band at fixed cooling rates. To apply, one simply plots the IR band intensity data in Fig. 4 and reads the cooling rate. The figure also shows that for a given cooling rate, the 452 mm^{-1} band intensity reaches a roughly constant value at high total H_2O, and there is even some indication that the 452 mm^{-1} band intensity decreases with further increasing total H_2O. This is in agreement with the quench-rate data of Silver et al. (1990) and in contrast with the isothermal equilibrium relation in which the OH concentration increases continuously with total H_2O (Ihinger et al., 1999), as expected.

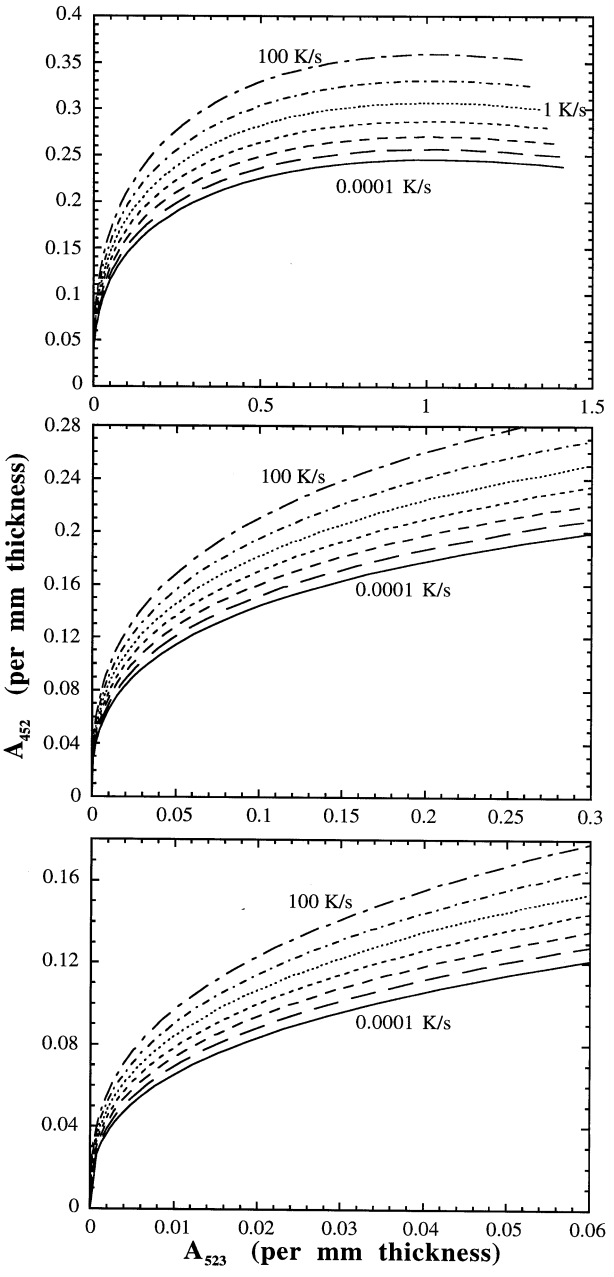

Fig. 4. The relation between the band intensity of the two bands and quench rate q. This diagram can be used to graphically obtain q at the apparent equilibrium temperature. Three figures are shown for application at low to high H_2O_t. The cooling rates between adjacent curves differ by a factor of 10.

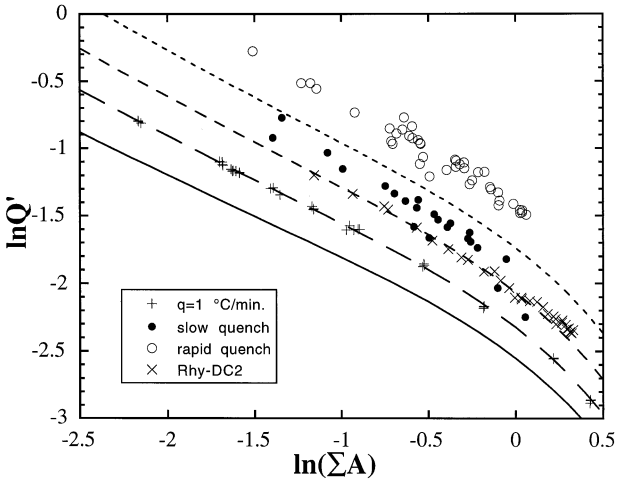

Fig. 5. The relation between $\ln Q'$ and $\ln \Sigma A$ for slow and rapid quench data (Silver et al., 1990) and for a diffusion experiment (one diffusion profile, Rhy-DC2, from Zhang and Behrens, 2000). Experimental data at 1.02 ± 0.05°C/min are shown for comparison so that data precision can be seen. The curves are the same as those in Fig. 2.

4.2. Quench Rates in Different Types of Experiments

Silver et al. (1990) reported quenched speciation of hydrous rhyolitic glasses after rapid and slow quench. The rapid-quench experiments were quenched by dropping the sample from the hot bomb into the water-filled cold bomb, and the quench rate was often referred to as ~200 K/s. The slow-quench experiments were quenched by taking the hot bomb out of the furnace and blasting compressed air onto the bomb, and the quench rate was often referred to as ~200°C/min. With our high-quality experimental data now covering quench rate up to 94 K/s, we can infer quench rates of these experiments with only small extrapolation from the measured species band intensities. In Fig. 5, slow and rapid quench data from Silver et al. (1990) are compared with our experimentally constrained curve (from Fig. 2). There is considerable scatter (about two orders of magnitude in terms of quench rate) for each set of the slow-quench and rapid-quench data. It is not clear why the scatter is so large, but possible reasons include (i) the poor operational reproducibility for slow quench (e.g., the intensity of the compressed air and the direction of the air blast relative to the bomb) and rapid quench (e.g., hesitation when the sample is dropped into the cold part of the bomb, and the size of the sample) and (ii) relatively large measurement errors of IR intensities for small samples due to the use of a previous-generation IR instrument. For most of their slow quench data, the inferred quench rate is about 9 K/s (Fig. 3), about the same as quench of a cm-sized sample directly in air (Xu and Zhang, 1999). For most of the rapid quench data, the average quench rate is ~1400 K/s (using Eqn. 5 for extrapolation), roughly comparable to the surface quench rate of a large chunk of melt dropped in water (Xu and Zhang, 1999).

Quenching in an internally heated pressure vessel is often accomplished by turning off power to the furnace (Behrens et al., 1996; Withers and Behrens, 1999; Zhang and Behrens, 2000). In order to obtain the quench rates for a sample quenched in an internally heated pressure vessel at the University of Hannover, the IR band intensities measured along a relatively long diffusion profile (Rhy-DC2, Zhang and Behrens, 2000) are plotted in Fig. 5. The precision of the data in terms of species concentrations is not high because the data are obtained for H_2O diffusion for which only total H_2O content is important. Nevertheless, the data follow a tightly defined curve, with cooling rate close to 1–2 K/s. The inferred cooling rate from the hydrous species is consistent with the recorded temperature–time history during quench with a cooling rate of about 100°C/min.

Cooling rates in a piston cylinder apparatus by turning off the power are directly measured in this work (59–94 K/s, see Table 1). Cooling rates in a rapid-quench cold seal bomb at the University of Hannover, which uses Ar gas as the quench medium, can be estimated from data of Zhang and Bebrens (2000) to be ~30 K/s at 500 MPa. It can be noted that quench rates in rapid-quench cold-seal bombs using water as quench medium and those using dense Ar gas as quench medium are very different (1000 vs. 30 K/s). Cooling rates for quench in water, in liquid nitrogen and in air have been investigated by Xu and Zhang (1999).

Combining all these data, we can rank experimental quenching rates as follows: q for rapid-quench cold-seal bombs at Caltech (water as quench medium) and for quench of a small sample in a large amount of water can be as high as ~1000 K/s; q for quench in the piston cylinder at the University of Michigan is ~70 K/s; q for rapid-quench cold-seal bombs at University of Hannover (dense Ar gas as quench medium) is ~30 K/s; q for quench of a cm-sized sample in liquid nitrogen is ~18 K/s (Xu and Zhang, 1999); q for air quench of an 8 mm size sample is ~12 K/s (Xu and Zhang, 1999); q for slow quench of cold-sealed bomb at Caltech is ~9 K/s; q for quench in internally heated pressure vessels at University of Hannover is 1–2 K/s. Experimental quench rates can vary from the above depending on how the apparatus is set up and how quench is accomplished, and on parameters such as the experimental pressure, the temperature of interest (apparent equilibrium temperature), the size of the sample, and/or the position of the sample.

4.3. Quench Rate of Natural Samples

The refined calibration of the geospeedometer based on H_2O species concentrations is used to calculate the cooling rates of natural pyroclasts. Figure 6A shows cooling rates calculated for a few hundred analyses of natural rhyolitic glasses, most are Mono Crater pyroclasts from one single site but different layers. These were collected by Zhang et al. (1995) and have been analyzed over the years in this laboratory. Also shown in Fig. 6A are natural rhyolitic glasses from the collection of Caltech laboratory (analyzed in Zhang et al., 1991; 1995), among which some are pyroclasts, some are from lava flows, and some have origin that is not available anymore. Figure 6B is a histogram for cooling rates of Mono Crater pyroclasts alone. From Fig. 6B, the cooling rates of most pyroclasts follow a log-normal distribution. Only a small fraction of pyroclasts (~6%) have very low cooling rates that do not seem to belong to the log-normal distribution.

From both Figs. 6A,B, most pyroclasts have cooling rates of 8 ± 3 K/s (which may be referred to as the most probable

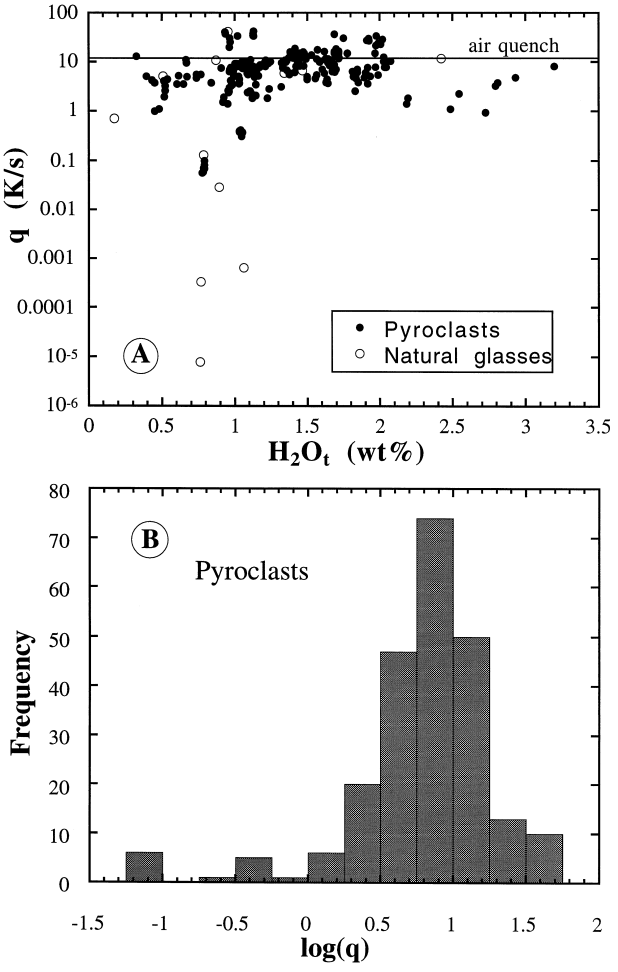

Fig. 6. (A) Cooling rates of natural pyroclasts collected from Mono Craters, shown as dots; and other natural glasses (from laboratory collections, some having origin not available anymore), shown as open circles. Since experimental cooling rates used to calibrate the geospeedometer ranges from 0.000 17 to 94 K/s, of all the inferred cooling rates in this diagram, only one sample with cooling rates of 8×10^{-6} K/s requires extrapolation (rather than interpolation). (B) Histogram for cooling rates of pyroclasts shown in (A).

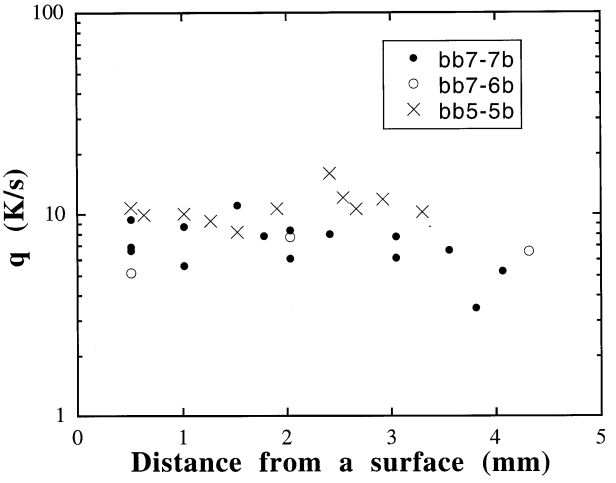

Fig. 7. Cooling rate of three natural pyroclasts from Mono Craters as a function of distance from a quench surface. Explanation of sample name: in the sample bb7-7b, bb means site bb, the subsequent 7 means layer 7, and 7b after the dash means fragment b of the 7th piece (which is cut into fragments a, b, c, etc.).

cooling rate), almost the same as cooling of cm-size clasts in stagnant air (12 K/s). This most probable cooling rate is likely due to cooling in the eruption column. For a hot erupting column to cool so rapidly (almost as rapid as in stagnant ambient air), entrainment of ambient air must be very effective in cooling down the column. The magnitude of the eruption may also affect the cooling rate in the erupting column. Most of the variability in the observed cooling rates can be attributed to variable clast size and to variable cooling rates in the dynamic erupting column. The small fraction of pyroclasts (~6%) outside the log-normal distribution and with cooling rates as low as 0.1 K/s probably cooled in the conduit and was later brought up by the next eruption without significant overheating to erase the earlier thermal signal (Newman et al., 1988; Zhang et al., 1995). If these interpretations are correct, the geospeedometer developed in this work provides a tool to distinguish the cooling environment of individual pyroclasts (in the erupting column, or in the erupting conduit). Furthermore, cooling rates of a given eruption column inferred from the geospeedometer may provide constraints on modeling and understanding of the eruption column.

For the rest of the natural glasses (the exact origin for some is not available anymore) shown in Fig. 6, some have cooling rates as low as 8×10^{-6} K/s. Such low cooling rates can be achieved for a melt about 10 m deep in a lava flow or in an eruption conduit.

In addition to measurements on random points of many pyroclasts, we also determined species concentration profiles in some large pyroclasts from Mono Craters to examine whether the interior cooling rates are the same as or lower than the surface cooling rates. First we identify an original pyroclast surface as a dull surface (not a conchoidal fracture surface). Then a profile perpendicular to the original surface is measured to determine whether cooling rates varied as a function of distance from the cooling surface. If there is a relatively large difference between surface and interior cooling rates, it would mean that true cooling rates in an erupting column must be determined using either small pyroclasts, or measurement near original surfaces of pyroclasts. Figure 7 shows three cooling rate profiles. Because the degree of transparency is low at some points, the analytical error is slightly greater for these samples than in experiments where only transparent samples are used or only transparent regions are measured. The average cooling rate is well constrained to be ~8 K/s. Within the analytical uncertainty, the cooling rate does not change from the surface to the interior of ~3.5 mm distance from the surface. That is, the interior can keep pace with surface cooling. Beyond this distance, cooling of the interior by heat conduction may not keep pace with surface cooling. This is roughly consistent with heat conduction calculations (Xu and Zhang, 1999).

4.4. Comparison of Controlled Cooling Rate Approach and Isothermal Approach

After investigating the kinetics of the hydrous species reaction for the development of a geospeedometer using two ap-

proaches, isothermal kinetic experiments (which can be referred to as chemists' approach) and controlled cooling rate experiments (which can be referred to as geochemists' approach), we summarize advantages and disadvantages of each method below.

If the main purpose is to understand the reaction rate law and reaction mechanism, isothermal experimentation is superior. Even complicated reaction rate laws and mechanisms can be inferred from isothermal kinetic investigations (Zhang et al., 1995; many classic examples in chemistry). Controlled cooling rate experiments, however, can only be used indirectly to infer the reaction rate law (Zhang et al., 1997a) and cannot be used to infer complicated reaction rate laws or reaction mechanisms.

If the main purpose is to calibrate a practical geospeedometer, there are four advantages of using the cooling-rate experimental approach instead of the isothermal experimental approach.

(i) Calibration of geospeedometer using the cooling-rate data is direct (cooling rate is directly related to species concentrations), but indirect using isothermal data.

(ii) With the use of piston-cylinder apparatus, experimental calibration can be conducted for a larger range of time scales using the controlled cooling rate experiments (6 orders of magnitude; 6 seconds to 2 months) than the isothermal experiments (4 orders of magnitude; 600 seconds to 2 months). Because isothermal experiments require several different durations (a time series) to examine how the species concentrations change from disequilibrium to equilibrium, and because it takes time to heat up (30–60 s) so each heating period must be at least this long, only when the reaction time scale is in the order of 10 minutes or longer, can the reaction rate constant at a given temperature be constrained well.

(iii) Controlled cooling rate experiments are more efficient: To investigate the response of the reaction to a given cooling rate, only one experiment is necessary. To constrain the reaction rate constant at a given temperature, five or more experiments are needed if equilibrium is approached from one side, and 10 or more experiments are needed if equilibrium is approached from both sides.

(iv) From our experience, controlled cooling rate experiments have slightly better reproducibility than isothermal kinetic experiments (comparing data in Zhang et al., 1995 vs. data in Zhang et al., 1997a and this work). The lower reproducibility for isothermal kinetic experiments is probably owing to temperature inaccuracy and fluctuation, and the inaccuracy in experimental duration because the heating-up and cooling-down durations are not exactly known.

The combination of both isothermal kinetic experiments and controlled cooling rate experiments provides a cross check to each other and hence is best for the accurate calibration of a geospeedometer.

5. CONCLUSIONS

The hydrous species geospeedometer in rhyolitic glass has been improved with new experimental data performed under controlled cooling rates in a piston-cylinder apparatus. Previous experimental data and those reported in this work together cover cooling rates of 0.000 17 to 94 K/s, and H_2O_t of 0.5 %–7.7 %. Therefore, little extrapolation is required for application to infer cooling rates of hydrous rhyolitic glasses of pyroclasts, lava flows and melt inclusions in phenocrysts. Furthermore, the geospeedometer is insensitive to pressure variations at $\leq$500 MPa.

The improved geospeedometer can be applied to infer cooling rate of a small rhyolitic glass sample, and the variation of cooling rates from one position to another with a spatial resolution of less than 0.5 mm (depending on the IR instrument). One class of future applications is to systematically sample (with well-controlled positions) pyroclastic beds, lava domes, or lava flows, to investigate the relation of cooling rates with sample position so as to unravel the thermal history and help understand the rich details of volcanological processes.

Acknowledgments—We thank A. T. Anderson, J. Ganguly and an anonymous reviewer for comments, and Raleigh Belcher, Juleen Jenkins, Yang Liu, Heidi Scharich, and Wenbing Yu for the analyses of some of the pyroclasts in Fig. 6. This research is funded by NSF Grants Nos. EAR-9458368 and EAR-9706107 and German DAAD.

Editorial handling: M. S. Ghiorso

REFERENCES

Behrens H., Romano C., Nowak M., Holtz F., and Dingwell D. B. (1996) Near-infrared spectroscopic determination of water species in glasses of the system $MAlSi_3O_8$ (M = Li, Na, K): an interlaboratory study. *Chem. Geol.* **128,** 41–63.

Ganguly J. (1982) Mg–Fe order–disorder in ferromagnesian silicates II: Thermodynamics, kinetics and geological applications. In *Advances in Physical Geochemistry* (ed. S. K. Saxena), Vol. 2, pp. 58–99. Springer-Verlag.

Ganguly J., Yang H., and Ghose S. (1994) Thermal history of mesosiderites: Quantitative constraints from compositional zoning and Fe–Mg ordering in orthopyroxenes. *Geochim. Cosmochim. Acta* **58,** 2711–2723.

Ihinger P. D., Zhang Y., and Stolper E. M. (1999) Speciation of water in rhyolitic glasses. *Geochim. Cosmochim. Acta* **63,** 3567–3578.

Mueller R. F. (1967) Kinetics and thermodynamics of intracrystalline distributions. *Mineral. Soc. Am. Spec. Pap.* **2,** 83–93.

Newman S., Stolper E. M., and Epstein S. (1986) Measurement of water in rhyolitic glasses: Calibration of an infrared spectroscopic technique. *Am. Mineral.* **71,** 1527–1541.

Newman S., Epstein S., and Stolper E. M. (1988) Water, carbon dioxide, and hydrogen isotopes in glasses from the ca. 1340 A.D. eruption of the Mono Craters, California: Constraints on degassing phenomena and initial volatile content. *J. Volcanol. Geotherm. Res.* **35,** 75–96.

Silver L., Ihinger P. D., and Stolper E. (1990) The influence of bulk composition on the speciation of water in silicate glasses. *Contrib. Mineral. Petrol.* **104,** 142–162.

Stolper E. (1982a) The speciation of water in silicate melts. *Geochim. Cosmochim. Acta* **46,** 2609–2620.

Stolper E. M. (1982b) Water in silicate glasses: An infrared spectroscopic study. *Contrib. Mineral. Petrol.* **81,** 1–17.

Withers A. C. and Behrens H. (1999) Temperature induced changes in the NIR spectra of hydrous albitic and rhyolitic glasses between 300 and 100 K. *Phys. Chem. Mineral.* **27,** 119–132.

Withers A. C., Zhang Y., and Behrens H. (1999) Reconciliation of experimental results on H_2O speciation in rhyolitic glass using in situ and quenching techniques. *Earth Planet. Sci. Lett.* **173,** 343–349.

Xu Z. and Zhang Y. (1999) Quantification of quench rates in water, air and liquid nitrogen. Goldschmidt Conference Abstract (Boston) 332.

Zhang Y. (1994a) Reaction kinetics, geospeedometry, and relaxation theory. *Earth Planet. Sci. Lett.* **122,** 373–391.

Zhang Y. (1994b) Temperature and pressure dependence of the speciation of water in rhyolitic glasses. *Eos* **75,** 54.

Zhang Y. (1999) H_2O in rhyolitic glasses and melts: Measurement, speciation, solubility, and diffusion. *Rev. Geophys.* **37,** 493–516.

Zhang Y. and Behrens H. (2000) H_2O diffusion in rhyolitic melts and glasses. *Chem. Geol.* in press.

Zhang Y., Stolper E. M., and Wasserburg G. J. (1991) Diffusion of water in rhyolitic glasses. *Geochim. Cosmochim. Acta* **55,** 441–456.

Zhang Y., Stolper E. M., and Ihinger P. D. (1995) Kinetics of reaction $H_2O + O = 2OH$ in rhyolitic glasses: Preliminary results. *Am. Mineral.* **80,** 593–612.

Zhang Y., Jenkins J., and Xu Z. (1997a) Kinetics of the reaction $H_2O + O = 2OH$ in rhyolitic glasses upon cooling: Geospeedometry and comparison with glass transition. *Geochim. Cosmochim. Acta* **61,** 2167–2173.

Zhang Y., Belcher R., Ihinger P. D., Wang L., Xu Z., and Newman S. (1997b) New calibration of infrared measurement of water in rhyolitic glasses. *Geochim. Cosmochim. Acta* **61,** 3089–3100.